Influence of Cold Pools Downstream of Mountain Barriers on Downslope Winds and Flushing

TSENGDAR J. LEE AND ROGER A. PIELKE
Department of Atmospheric Sciences, Colorado State University, Fort Collins, Colorado

ROBERT C. KESSLER
Systems Applications, Inc., San Rafael, California

JOHN WEAVER
NOAA/NESDIS/RAMM, Fort Collins, Colorado

(Manuscript received 20 May 1988, in final form 30 March 1989)

ABSTRACT

The influence of cold pools downstream of mesoscale mountain barriers on downslope winds and flushing is investigated in this study by means of a numerical mesoscale model. The model is compared with existing analytical and numerical solutions. It is found that the numerical model produces phases and amplitudes of nonlinear mountain waves reasonably well.

The solutions show that the structure of mountain waves can be modified greatly by the presence of the cold pool. When a cold pool is present downstream of the mountain, the development of a large amplitude mountain wave is inhibited. In the absence of surface heating, downslope winds associated with a mountain wave can be prevented from penetrating the cold pool to reach the surface and flush out the very stable cold air, particularly when the synoptic pressure gradient is oriented so as to continuously replenish the cold air. Results also suggest that shear-induced turbulent mixing at the top of the cold air has little effect on flushing. Based on the observations and the numerical results, in the absence of significant surface heating a favorable large-scale surface-pressure gradient force must be involved to remove the cold pool before the downslope winds can actually reach the surface.

1. Introduction

Air masses on different sides of a mountain barrier can have different thermal stratifications especially when one air mass is blocked by the mountain. In northeast Colorado, for instance, outbreaks of a polar high can often be blocked and dammed by the Rocky Mountains. In addition, if the ground is covered by snow and the sky is clear, radiative cooling can even intensify the accumulation of cold air in this area. It is often observed that a deep surface inversion remains in this area for a period of time. Although the wind aloft can be strong, the surface is insulated by this stable and relatively stagnant cold pool. Once this cold pool is removed, strong downslope wind can reach the surface, melt the snow, and sometimes cause damage. This study investigates the influence of this pool of cold air on downslope winds and the flushing of the cold air east of the mountain barrier.

Downslope winds have been studied extensively for the last several decades, however, there is still no agreement on a unique physical mechanism that is responsible for the development of severe lee slope windstorms. As summarized by Durran (1986), three mechanisms have been proposed to account for the development of strong lee slope winds. They are based on linear theory, hydraulic theory, and on the results from numerical simulations.

The *linear theory* gives a clear picture of the tuning of waves in a continuously stratified atmosphere where the upward propagating waves are reflected from a layer in which the Scorer parameter changes rapidly with height. When the multilayered atmosphere is tuned to give a maximum response, the superposition of upward and downward propagating waves will cause a large amplitude perturbation on the lee slope of a mountain and a very strong wind will be experienced at the surface. However, the application is limited because the theory cannot apply to large amplitude waves where nonlinear effects become very important.

Hydraulic theory predicts that strong winds will occur when the air flow transits from subcritical to supercritical flow while passing the mountain crest, but the theory is not complete when applied in the atmosphere. In classic hydraulic jump theory a rigid lid or

---

Corresponding author address: Tsengdar J. Lee, Dept. of Atmospheric Sciences, Colorado State University, Fort Collins, CO 80523.

free surface limits upward propagating gravity waves; such a feature does not exist in the atmosphere. In Durran's 1986 paper, a generalized hydraulic jump phenomenon was proposed to link the linear theory with the hydraulic theory. He suggested that the energy within the upward propagating gravity waves can be trapped below a low level inversion and a hydraulic jump results where the role of surface waves in the hydraulic theory is replaced by internal gravity waves. Smith (1985) proposed a generalized internal hydraulic theory where the upper reflective boundary condition in the classic hydraulic theory is replaced by a mean-state critical layer, where the mean flow reverses its direction. A steady state hydraulic jump can be found at the lee of the mountain beneath the critical layer based on his theory. A series of numerical experiments by Durran and Klemp (1987), and Bacmeister and Pierrehumbert (1988) have successfully replicated this generalized theory proposed by Smith and showed that a high drag state can be found when there is a mean state critical layer present.

Numerical investigations offer a large number of choices of boundary conditions, stabilities, and different terrain configurations. Based on numerical results, Clark and Peltier (1977, 1984), and Peltier and Clark (1979) have suggested that wave-breaking is important and, using the linear theory of wave reflection, they suggested that the upward propagating wave energy is reflected from a self-induced critical layer where the amplitude of mountain waves is so large that a locally reversed flow associated with breaking waves and strong mixing is found. This result can be used to explain situations when the flow is very nonlinear but it is difficult to interpret since the physical explanation relies predominately on the linear theory. Although Smith's theory can be used to support Clark and Peltier's result, there is still a fundamental difference between the two theories since Smith's analysis is based on a preexisting reflective upper boundary condition while Clark and Peltiers' theory is based on wave reflection from a critical level which develops during the evolution of the flow. However, it is confirmed that the breaking wave is crucial to maintain the existence of high wave drag due to the presence of the irregular terrain.

The flushing mechanism, on the other hand, has received less attention. Pielke (1985) suggested that, in the absence of surface heating, two possible interactions may be important to flush out cold air downwind of a mountain barrier. In the first case, the horizontal wavelength of air motions must be close to the characteristic horizontal wavelength of the terrain in order to remove the cold air. In the second case, the cold air could be mixed out by the shear-induced turbulence at the top of the cold pool. Mahrer and Pielke (1978) also reported that the mountain wave structure is very different in the lower troposphere when considering surface interactions. This raises the question: When there is a surface based inversion, how can mountain waves actually penetrate the stable layer? The cold and stable air will also modify the form of the mountain waves and a high drag state may not be present at all. Based on data collection in Fort Collins, Colorado (see Appendix), a favorable orientation of the synoptic scale systems is necessary for the presence of severe downslope winds. It is also observed, after a polar outbreak along the Colorado Front Range, that the cold air can remain in this area when a downslope wind is not present. The interaction between the cold pool and the mountain waves and the necessary conditions to remove the cold pool are discussed in this paper.

2. The numerical model

The numerical simulations in this study are obtained by using a two-dimensional version of the Colorado State University Mesoscale Model (Pielke 1974; Mahrer and Pielke 1977; McNider and Pielke 1981). The model is hydrostatic and has previously been modified to predict air flow over a two-dimensional mountain barrier (e.g., Hoinka 1985). A terrain-following coordinate system (x, y, z^*) is used in this model; however, unlike the Mahrer and Pielke (1977) version, scaling is done to a fixed height $\bar{s}$, such that

$$z^* = \frac{\bar{s}(z - z_G)}{(\bar{s} - z_G)}. \qquad (1)$$

The height $\bar{s}$ is the initial elevation of a material surface s which is assigned to be the top of the model; z_G is the height of the terrain. When there is no diabatic forcing the governing equations of momentum, continuity and potential temperature are the following:

$$\frac{du}{dt} = fv - fV_g - \theta\frac{\partial\pi}{\partial x} + g\frac{z^* - \bar{s}}{\bar{s}}\frac{\partial z_G}{\partial x} + \left(\frac{\bar{s}}{\bar{s} - z_G}\right)^2 \times \frac{\partial}{\partial z^*}\left(K_z{}^m\frac{\partial u}{\partial z^*}\right) + \frac{\partial}{\partial x}\left(K_H\frac{\partial u}{\partial x}\right), \qquad (2)$$

$$\frac{dv}{dt} = fU_g - fu + \left(\frac{\bar{s}}{\bar{s} - z_G}\right)^2 \times \frac{\partial}{\partial z^*}\left(K_z{}^m\frac{\partial v}{\partial z^*}\right) + \frac{\partial}{\partial x}\left(K_H\frac{\partial v}{\partial x}\right), \qquad (3)$$

$$\frac{d\theta}{dt} = -v\frac{\partial\bar{\theta}}{\partial y} + \left(\frac{\bar{s}}{\bar{s} - z_G}\right)^2 \times \frac{\partial}{\partial z^*}\left(K_z{}^\theta\frac{\partial\theta}{\partial z^*}\right) + \frac{\partial}{\partial x}\left(K_H\frac{\partial\theta}{\partial x}\right), \qquad (4)$$

$$\frac{\partial u}{\partial x} + \frac{\partial w^*}{\partial z^*} - \frac{1}{\bar{s} - z_G}\left(u\frac{\partial z_G}{\partial x}\right) = 0, \qquad (5)$$

$$\frac{\partial\pi}{\partial z^*} = -\frac{\bar{s} - z_G}{\bar{s}}\frac{g}{\theta}, \qquad (6)$$

where π is the Exner function and is defined by

$$\pi = c_p\left(\frac{p}{p_{00}}\right)^{R/c_p}. \quad (7)$$

The vertical velocity and the total derivative are defined by

$$w^* = \frac{\bar{s}}{\bar{s} - z_G} w + \frac{z^* - \bar{s}}{\bar{s} - z_G}\left(u\frac{\partial z_G}{\partial x}\right), \quad (8)$$

$$\frac{d}{dt} = \frac{\partial}{\partial t} + u\frac{\partial}{\partial x} + w^*\frac{\partial}{\partial z^*}. \quad (9)$$

One should notice that only the mesoscale pressure gradient has a contribution to the term $\theta^{-1}\partial\pi/\partial x$ in Eq. (2) (appendix A, McNider and Pielke 1981). Also, an overbar on a variable indicates a constant prescribed value [e.g., $\partial\bar{\theta}/\partial y$ in (4)]. The mountain profile is a "witch of Agnesi,"

$$z_s(x) = \frac{ha^2}{x^2 + a^2}, \quad (10)$$

where a is the mountain half width and h the mountain height. For cases with a higher mountain, an improved technique of pressure gradient force calculation suggested by Mahrer (1984) is utilized. In order to emulate a radiative top boundary condition a Rayleigh friction layer of the type described by Durran and Klemp (1982) is added at the top of the model, which can prevent the upward propagating gravity waves from erroneously reflecting back downward. A free-slip bottom boundary condition is applied at the surface. The radiative boundary suggested by Klemp and Lilly (1978) is used at the lateral boundaries. The model has a subgrid-scale mixing parameterization for a stably stratified atmosphere as reported by McNider and Pielke (1981). The vertical exchange coefficient, when using this scheme, is a function of local Richardson number. We use this scheme to parameterize the turbulent mixing when the mountain wave overturns. In order to maintain nonlinear stability, a highly selective z^*-parallel filter, as described in Mahrer and Pielke (1978), is applied to the perturbation u and θ fields. The equivalent exchange coefficient of this filter is a function of wavelength and a value for the coefficient is given in section 3.

The model is initialized with a homogeneous east–west mean potential temperature field and a mesoscale potential temperature perturbation is superposed on the mean field when a cold pool is present. The horizontal wind field is initialized with its geostrophic value and a geostrophic wind shear across three vertical grids is assigned at the top of the cold pool. Since the mean-state horizontal pressure gradient force is replaced by a Coriolis force term, as shown in Eqs. (2) and (3), geostrophic wind balance is automatically enforced. A longitudinal potential temperature gradient, $\partial\bar{\theta}/\partial y$, is required, as shown in Eq. (4), to achieve thermal wind balance when vertical geostrophic wind shear is present. The mesoscale pressure field is obtained by integrating the hydrostatic relation [Eq. (6)] downward from the top of the model.

3. Test of the model

Analytical solutions for specific flow configurations are available from a number of investigators (Lilly and Klemp 1979; Miles and Huppert 1969). The model used in this investigation has been successfully tested against analytical solutions and observed flows by Hoinka (1985). Although the Boussinesq approximation is not made in this version, a significant departure from Hoinka's work is not expected.

Our first test is to reproduce finite amplitude mountain waves first reported by Klemp and Lilly (1978). In this case a stratified two-layer atmosphere is introduced. The atmosphere has a temperature lapse rate of $\Gamma = -6°\mathrm{C\ km^{-1}}$ in the first 10 km above the ground which is similar to the average lapse rate in the troposphere. From 10 km up to 20 km an isothermal stratosphere is introduced which also serves as an absorbing layer. In this experiment the model has 81×50 grid points and a mountain of 1 km height is centered at the horizontal grid number 41. The mountain half-width, a, is 20 km. The horizontal grid spacing is 4 km and the vertical grid spacing is 333 m in the troposphere and 500 m in the stratosphere. The filter is equivalent to $K_H = 1 \times 10^4\ \mathrm{m^2\ s^{-1}}$ for a $4\Delta x$ wave. The model is integrated to a dimensionless time of $\bar{u}t/a = 57.6$ to achieve a steady state solution. Figure 1a illustrates the perturbation of the potential temperature field and the contours of horizontal velocity. A strong mountain wave structure similar to Klemp and Lilly's result (Fig. 1b) is observed in the figure. The horizontal velocity is not as high (i.e., maximum of 32 m s^{-1} in Klemp and Lilly's work and 28 m s^{-1} in ours) probably because of the filter.

Most of the previous studies have assumed that the rotational effect of the earth is negligible for the space and time scales used in this study. Scale analysis (Pielke 1984) suggests that the Coriolis effect should be unimportant when the Rossby number, $\mathrm{Ro} = \bar{u}/fa \gg 1$. Since Ro is inversely proportional to mountain half length, a, the wider the mountain the more important the Coriolis rotational effect should be. Based on more detailed scale analysis, Pierrehumbert and Wyman (1985) concluded that the upstream deceleration is on the order of O(Fr) for large Ro and O(Ro Fr) for small Ro. Here $\mathrm{Fr} = Nh/\bar{u}$ is the inverse Froude number and N is the Brunt–Väisälä frequency which is defined as

$$N^2 = \frac{g}{\bar{\theta}}\frac{\partial\bar{\theta}}{\partial z}. \quad (11)$$

Also, their results show that the Coriolis force limits

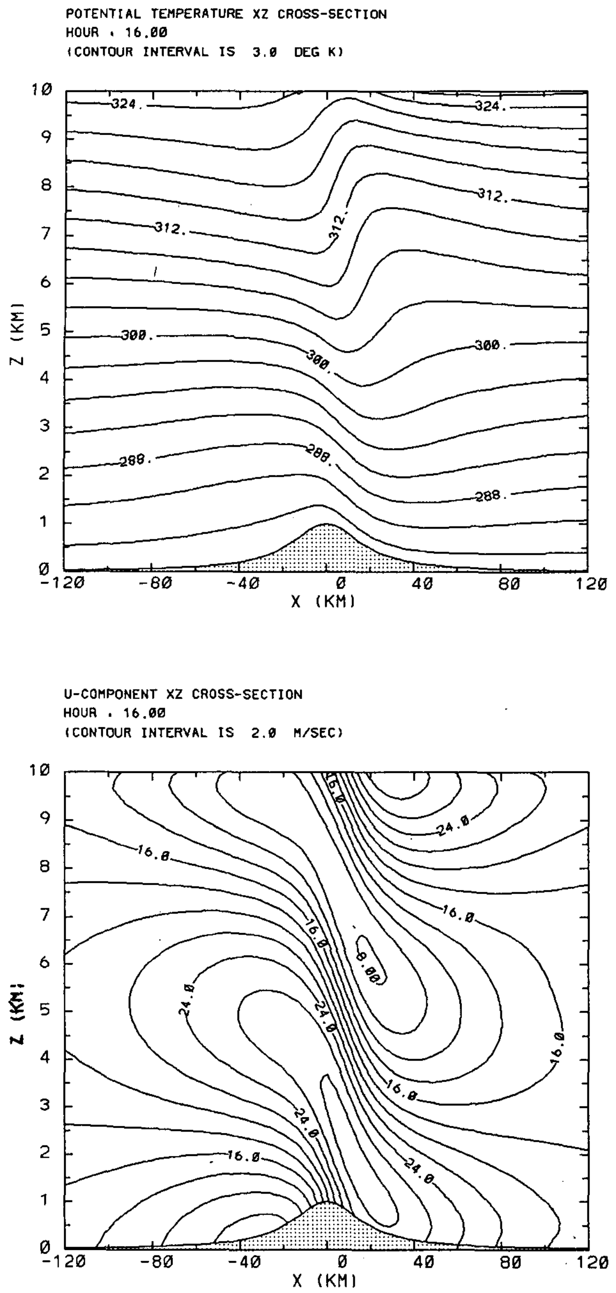

FIG. 1a. Numerical solution for (a) isentropes and (b) contours of horizontal velocity at $\bar{u}t/a$ = 57.6 for a two-layer atmosphere flowing over a mountain with h = 1000 m, $\Gamma = -6°\mathrm{C\ km}^{-1}$ below 10 km and isothermal aloft.

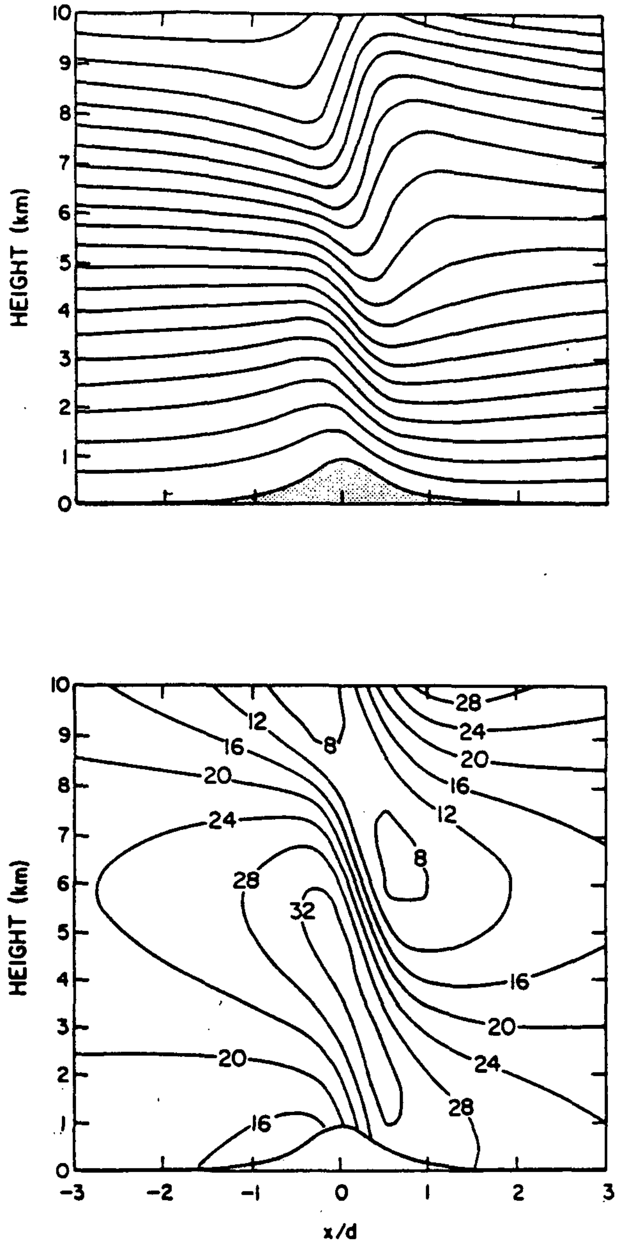

FIG. 1b. As in Fig. 1a except simulation from Klemp and Lilly (1978) and $\bar{u}t/d$ = 50, in which $d = 2a$; (d can be taken as 40 km for comparison).

the upstream extent of the decelerated layer. The maximum upstream extent of this layer is on the order of the deformation radius Nh/f. To isolate this rotational effect, an experiment was designed to have the same setup as in Fig. 1a except with the inclusion of the Coriolis force at 40°N. The Rossby number in this experiment is Ro = 10.67 and the inverse Froude number is Fr = 0.55. The deceleration of horizontal velocity should be on the order of Fr. The numerical result at $\bar{u}t/a$ = 57.6 is shown in Fig. 2. The horizontal deceleration of wind speed is approximately as estimated and the upstream extent is rather limited (almost one radius of deformation as predicted). As compared to Fig. 1a, the locations of the maximum and minimum winds are found to occur at higher elevations. The differences in mountain wave amplitude must be attrib-

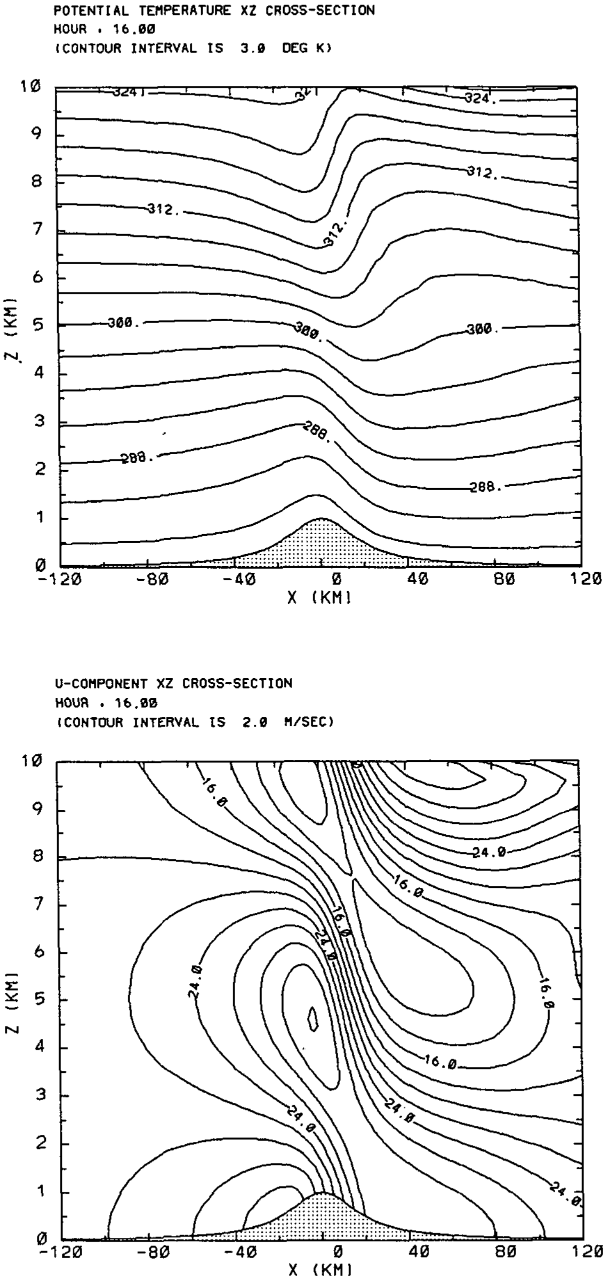

FIG. 2. As in Fig. 1a except with $f = 9.4 \times 10^{-5}$ s^{-1}.

utable to inertial oscillations. More importantly, the upstream inflow condition is modified by the presence of the Coriolis force and, consequently, must exert some influence on the amplitude of the mountain wave even when $\mathrm{Ro} \gg 1$.

As commented by Durran (1986), the two layered atmosphere test (Klemp and Lilly 1978) is not ideal since the atmosphere is not tuned to have a maximum response and the second layer is occupied by the viscous damping layer. We therefore performed a test with $N = 0.02$ s^{-1} in the lower troposphere and $N = 0.01$ s^{-1} in the upper troposphere. The interface is located at 3142 m which is expected to yield a minimum response as suggested by the linear theory. The model was set up to have 121×64 grid points and the mountaintop was centered at the horizontal grid number 61. The height of the mountain is 600 m and the half-width, in this case, is 10 km. The horizontal grid spacing is 1.5 km and the vertical grid spacing is 200 m in the first 8 km and 500 m aloft. A result very similar to Durran's Fig. 2 is obtained. In this simulation, a hydrostatic counterpart of a hydraulic jump is produced as shown in Fig. 3a, and Durran's figure is shown for comparison in Fig. 3b. This experiment documents that the model can successfully replicate the nonlinear response in a two layered atmosphere and suggests we should be able to realistically introduce a layer of cold air in the model.

4. The influence of a cold pool

With the presence of a cold pool downstream of a mountain barrier, the effective shape of the mountain should be modified by the cold and stable air. The mountain wave structure should therefore be very different as contrasted to when the cold pool is absent. To investigate this hypothesis, a cold pool is introduced downstream of a 2 km mountain which has a 20 km half-width. The geostrophic wind velocity is $U_g = 20$ m s^{-1}. The static stabilities are assigned to be $N = 0.012$ s^{-1} in the troposphere and $N = 0.02$ s^{-1} in the cold pool. As in the 1 km mountain tests described in the previous section, a typical wintertime stratosphere which starts at an elevation of 10 km and has a static stability of $N = 0.02$ s^{-1} is introduced at the top of the model. However, unlike that test, the absorbing layer starts from 15 km and extends to 30 km. Similar grid structure but with 200 m vertical resolution is utilized in the following tests.

The control experiment is a run without a cold pool. The inverse Froude number for the layer below 10 km in this case is 1.2 and is much larger than its critical value for the mountain wave to break. As expected, the wave overturns almost immediately after initialization and a strong windstorm is observed in the lee of the mountain. The wave first overturns near time $\bar{u}t/a = 7.2$ at a location near 8 km which is approximately three-fourths of the vertical wavelength. Here the vertical wavelength L is defined as

$$L = \frac{2\pi}{l}, \tag{12}$$

in which l is the Scorer parameter:

$$l^2 = \frac{N^2}{\bar{u}^2} - \frac{1}{\bar{u}} \frac{\partial^2 \bar{u}}{\partial z^2}. \tag{13}$$

The wave-breaking region then becomes larger and

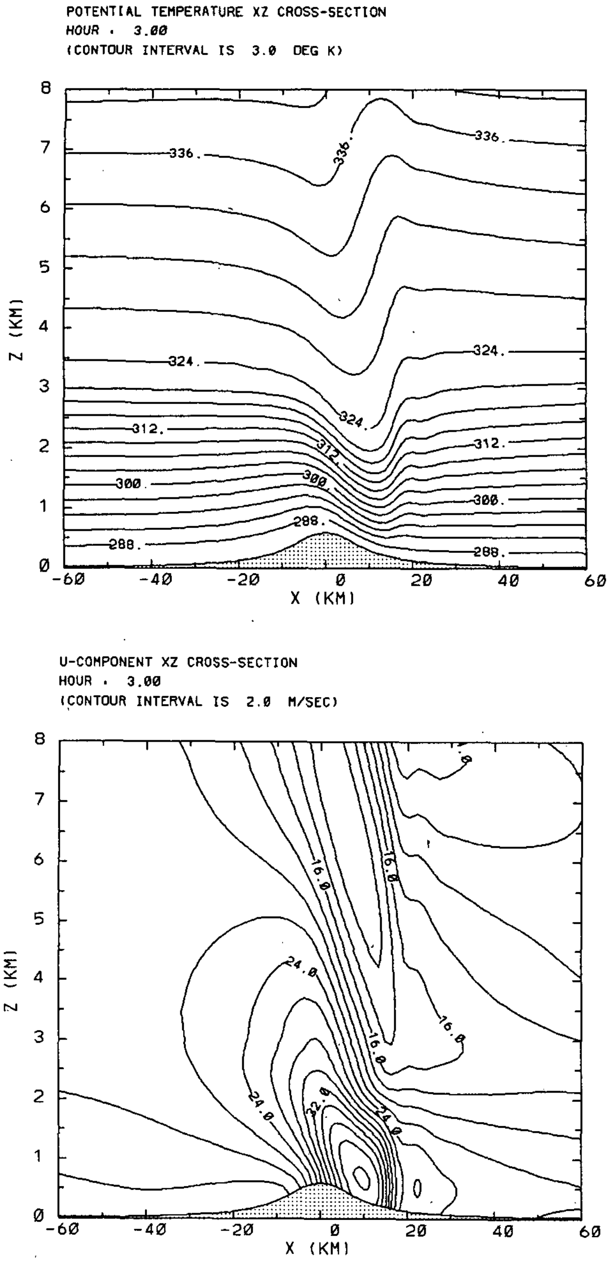

FIG. 3a. Numerical solution for (top) isentropes and (bottom) contours of horizontal velocity at $\bar{u}t/a$ = 21.6 for a two-layer atmosphere flowing over a mountain with h = 600 m, N = 0.01 s^{-1} below 3142 m and N = 0.02 s^{-1} aloft.

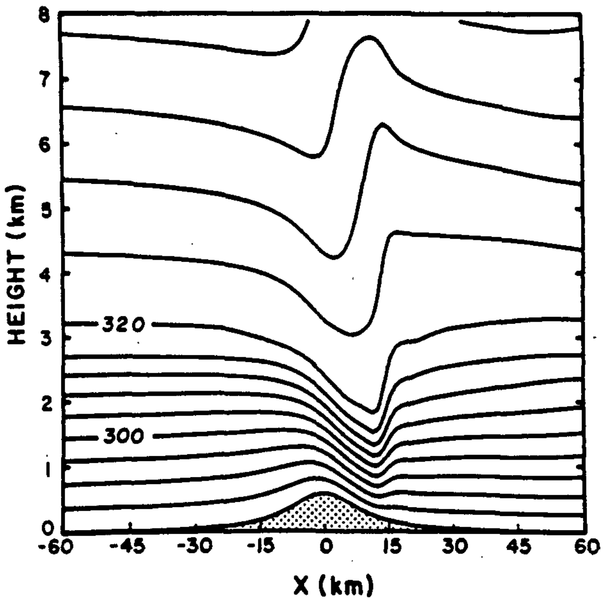

FIG. 3b. Numerical solution for isentropes at $\bar{u}t/a$ = 20 for a two-layer atmosphere flowing over a mountain with h = 600 m, N = 0.01 s^{-1} below 3142 m and N = 0.02 s^{-1} aloft; (from Durran 1986).

gradually moves downward and downstream. Figure 4 shows the isentropes and the horizontal velocity at $\bar{u}t/a$ = 14.4 and 28.8, some time after the wave first overturns. The upper level flow reverses its direction between 4 and 8 km after the wave overturns. At time $\bar{u}t/a$ = 14.4, a pattern similar to a hydraulic jump is found and the pattern is clearly a propagating hydraulic jump at $\bar{u}t/a$ = 28.8. The maximum horizontal wind speed is close to 50 m s^{-1} along the lee slope. This result shows that a high drag state can be found after the wave breaks. A similar result was first noticed by Clark and Peltier (1977) and they suggested that this self-induced critical layer acts like a reflector and results in a high drag state.

When a geostrophic wind is directed towards a mountain, however, the cold air can be dammed up against the terrain. We first show an experiment with a 2 km cold pool and a geostrophic wind in the cold pool of -10 m s^{-1}. A linear geostrophic wind shear is assigned beginning at the top of the cold pool with a depth of 400 m. This configuration is very similar to the situation that creates cold air damming in northeast Colorado except the wind shear is stronger here. In order to achieve thermal wind balance, the advection of mean state potential temperature, $-v\partial\bar{\theta}/\partial y$, was added to the right-hand side of Eq. 4. Figure 5 shows the numerical solution at $\bar{u}t/a$ = 28.8. It is easily seen that the cold air maintains its depth at this particular time and the wave amplitude is quite small. A very different flow structure than shown in Fig. 4 is found. To examine the hypothesis that the cold pool acts like topography, we replace the cold pool by a plateau with a shape similar to the cold pool. The solution is shown in Fig. 6. As we compare Figs. 5 and 6, it is found the solutions are very similar to each other, supporting the conclusion that the cold pool influences the air flow in a similar fashion as terrain of the same shape. It also demonstrates that shear induced turbulence at the top of the cold pool is ineffective at removing the cold pool

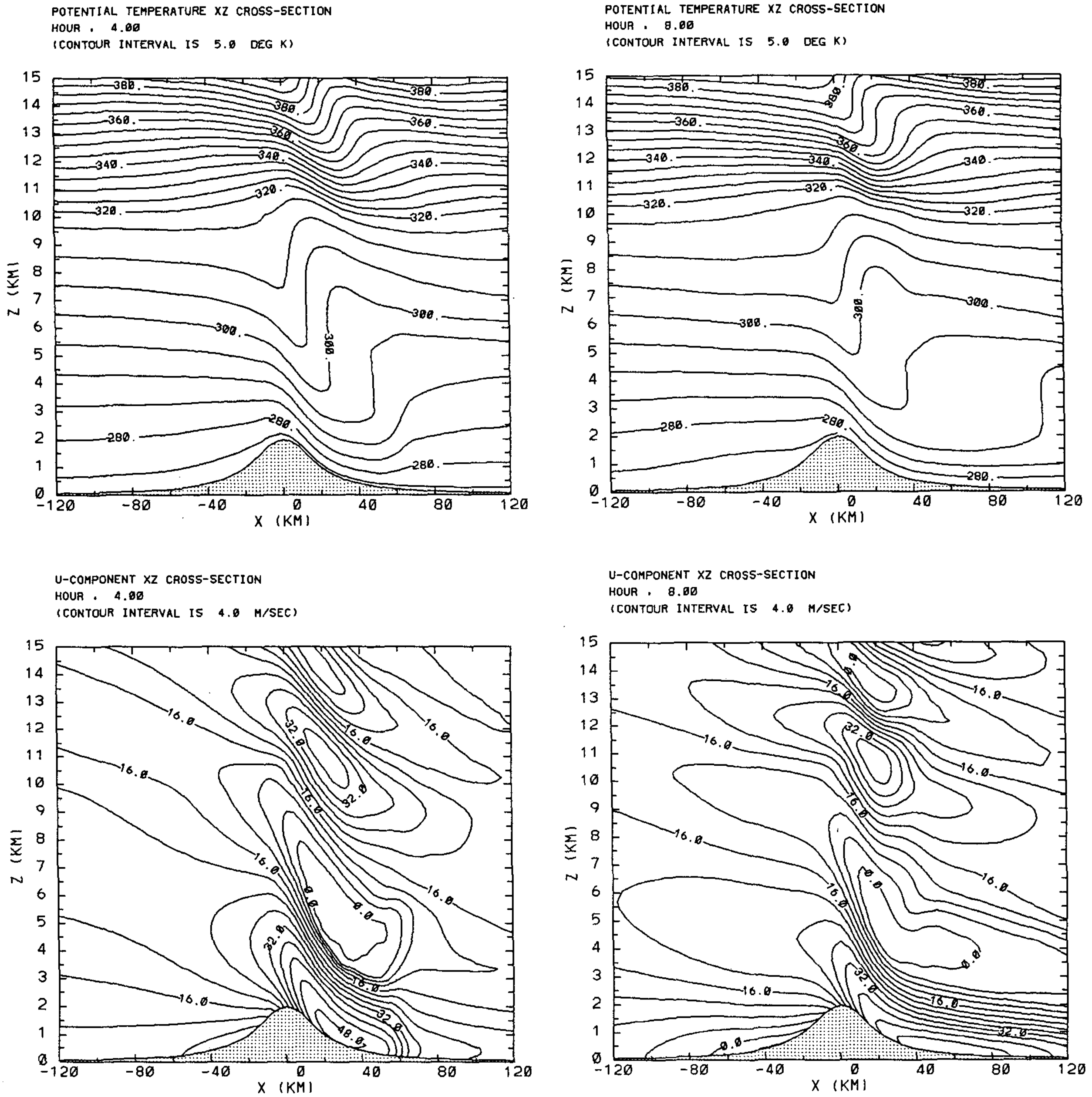

FIG. 4. Numerical solution for isentropes and contours of horizontal velocity at $\bar{u}t/a$ = 14.4 (left-hand panels) and 28.8 (right-hand panels) for a two-layer atmosphere flowing over a mountain with h = 2000 m, $f = 9.4 \times 10^{-5}$ s^{-1}, and $N = 0.012$ s^{-1} below 10 km and $N = 0.02$ s^{-1} aloft. The cross mountain flow is 20 m s^{-1} from the west.

(in fact shallow mixing across the cold pool will strengthen the inversion). Notice that the lifting of isentropic surfaces in Fig. 5 is due to the extra mass flux from the cold pool into the domain, which induces a net upward velocity and raises the isentropes.

An analytical solution of stratified airflow over irregular terrain has been obtained by Lilly and Klemp (1979) for a similar topographic shape to that shown in Fig. 6 using the following profile:

$$z_s(x) = \frac{h\left(\dfrac{x+a}{a}\right)}{1+\left(\dfrac{x+a}{a}\right)^2} + \frac{h}{2}, \qquad (14)$$

and an atmosphere static stability of $N = 0.012$ s^{-1}. Our steady state numerical and the analytical nonlinear solutions of hydrostatic mountain waves for the

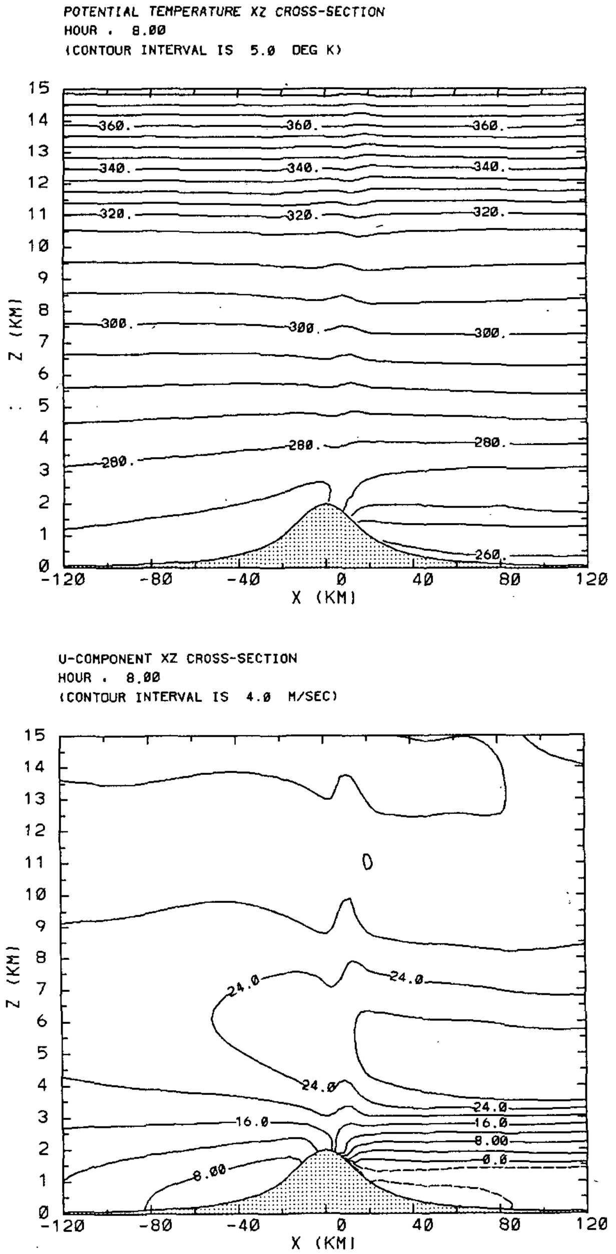

FIG. 5. As in Fig. 4 except a 2000 m deep cold pool with $N = 0.02$ s^{-1} and $U_g = -10$ ms^{-1} is introduced downstream of the mountain. This figure is shown at $\bar{u}t/a = 28.8$.

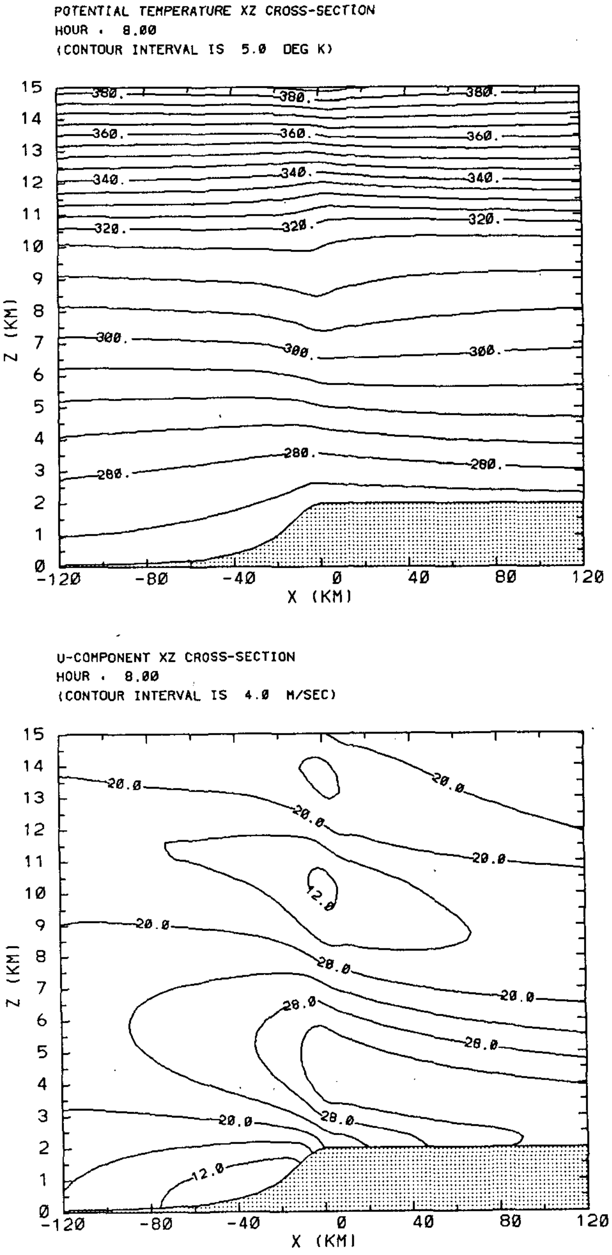

FIG. 6. As in Fig. 5 except the cold pool is replaced by a plateau with similar shape.

mountain profile given by (14) are plotted in Fig. 7. The good agreement between the two results further documents that the numerical model has the capability of replicating mountain waves above an asymmetric mountain. According to the analytical solution obtained by Lilly and Klemp, waves forced by this mountain profile should give a one-fourth phase shift as compared to the solution forced by a bell-shaped mountain. This yields a maximum response at a level of one vertical wavelength instead of three-fourths of the wavelength. Also, the maximum response should move from the lee slope to a location above the mountain crest. A similar phase shift is found in both Figs. 5 and 6. Although the numerical results in Figs. 5 and 6 are for a condition of a two-layer atmosphere and the depths of the cold pool in Fig. 5 slowly vary with time, the qualitative similarity between our numerical solution and the analytical solution appears to confirm

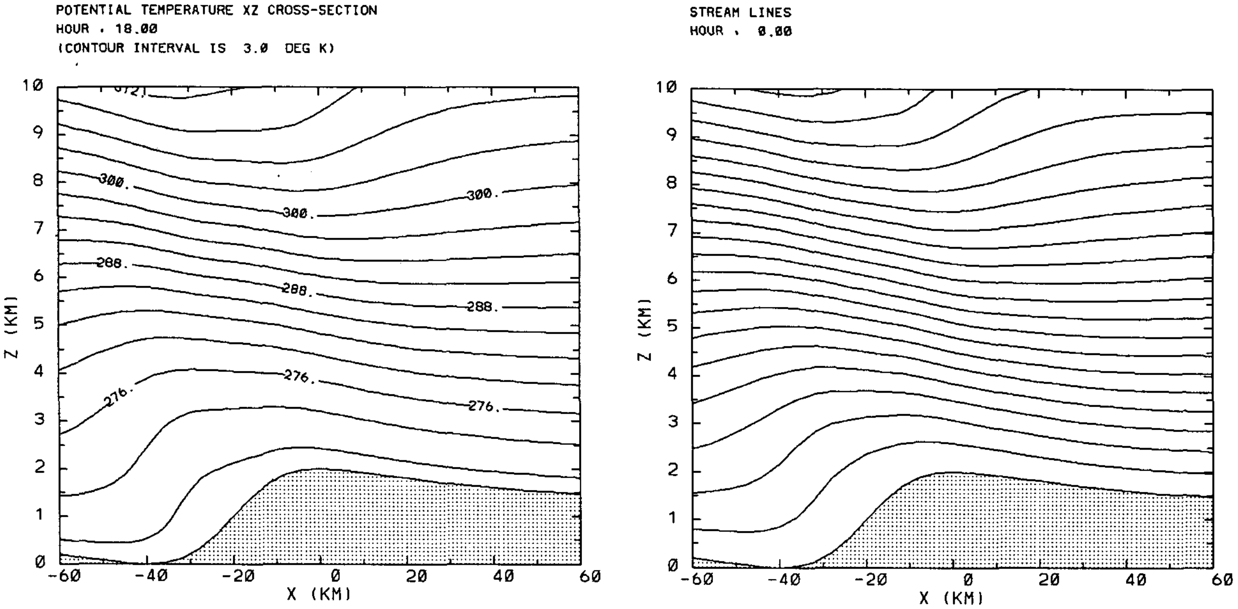

FIG. 7. Comparison of isentropes between (a) our numerical solution at $\bar{u}t/a = 64.8$ and (b) Lilly and Klemp's (1979) analytical solution for air flowing over an asymmetric mountain with $h = 2000$ m.

the hypothesis that the cold pool can act similar to terrain and the "effective" terrain height is a combination of the mountain and the cold pool.

When the geostrophic wind towards the terrain in the cold pool is not strong enough to maintain the depth of the cold pool, the solution is somewhat different, as compared to the $U_g = -10$ m s^{-1} simulation. We performed a test with $U_g = -5$ m s^{-1} with an initial cold pool depth of 2 km. Results of this experiment at $\bar{u}t/a = 28.8$ and 57.6 are illustrated in Fig. 8. It is seen in this figure that the cold pool is slowly eroded away although the wave does not break even after a long period of integration. The flow pattern is similar to subcritical flow everywhere in that a fluid column in the lower troposphere experiences an acceleration when it is passing the crest. It then decelerates and converts kinetic energy into potential energy after passing the crest. This is the reason the horizontal velocity field in this figure shows a maximum velocity core above the mountain crest. Notice a relatively high wind speed area above the cold pool where the cold pool acts like a mountain and the flow accelerates while passing over it. The isentropes at $\bar{u}t/a = 57.6$ show a drop in the potential temperature surface in the upper troposphere which is believed, according to Durran's recent study (1986), to act similar to the free surface in classical hydraulic theory. The forming of this subcritical flow pattern is not only attributed to the displacements of isentropic surfaces in the upper troposphere but also to the presence of the cold pool. Since a warm air parcel experiences a net upward buoyancy force when it interacts with the cold pool, it is not possible for the parcel to accelerate downstream as rapidly as it would in the absence of the cold pool.

The destabilization near the mountain crest level seen in Fig. 8 is due to the warm advection from the thermal wind effect (i.e., $v\partial\bar{\theta}/\partial y$) from the initial top of the cold pool up to 400 m above that level. By comparing this result to Fig. 4, it is seen that the development of finite amplitude mountain waves is confined in a narrow region near the top of the mountain where the cold air has been eroded away as a result of turbulence generated near the top of the cold pool. This turbulence is caused by the warm air undercutting air higher up in which no temperature advection occurred.

When the cold pool (with $U_g = -5$ m s^{-1}) is initially 1 km instead of 2 km, it is not deep enough to modify the mountain wave as much as found for the deeper cold pool. However, the development of finite amplitude waves is still retarded by the presence of the cold pool. The wave first breaks at a much later time (between a dimensionless time of 25.2 and 28.8), as compared to the simulation without the cold pool (see Fig. 4). The flow at the same times as in Fig. 8 is illustrated in Fig. 9. At $\bar{u}t/a = 28.8$ the amplitude of mountain wave is large enough to break and the hydraulic jump pattern begins to form. Eight hours later, at $\bar{u}t/a = 57.6$, the surface wind on the lee slope has exceeded 50 m s^{-1} and the flow resembles a propagating hydraulic jump and is similar to Fig. 4, although the near surface winds are somewhat larger at this time in Fig. 9. Strong vertical mixing and a relatively stagnant re-

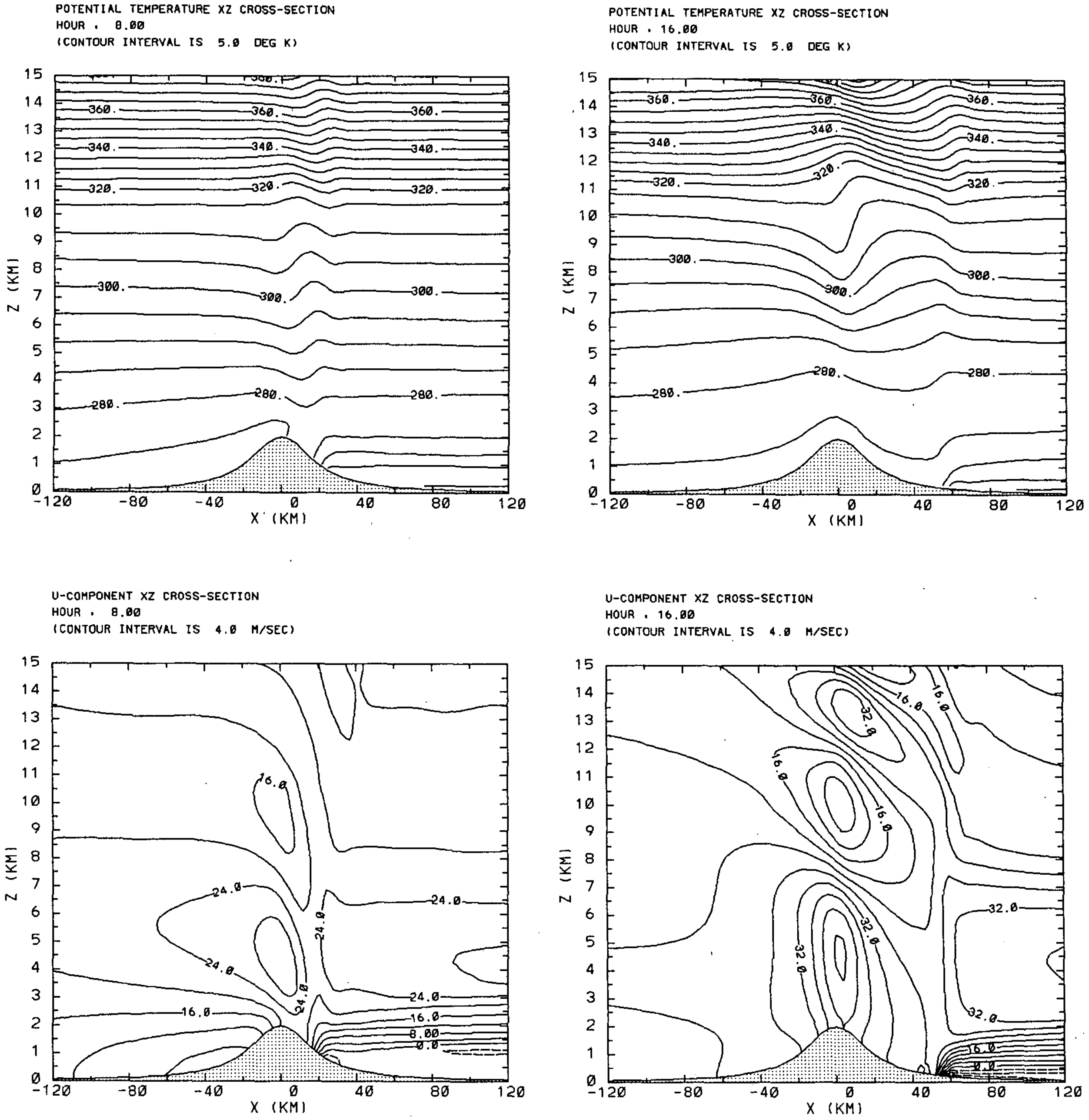

FIG. 8. As in Fig. 5 except at $\bar{u}t/a = 28.8$, and 57.6. Also, the geostrophic wind in the cold pool is $U_g = -5$ m s^{-1}.

gion is obvious above the maximum surface wind. This is very similar to the control experiment (Fig. 4) but it happens at a later time.

By comparing Fig. 9 to Fig. 8, it is noticed that the depth of the cold pool is crucial to the development of mountain waves. The deeper the cold pool, the more difficult it is for the amplitude of the wave to grow since the displacements of streamlines are minimized by the stable stratification when the cold pool is present. However, if we integrate the model to a sufficiently long time, the cold pool can be eroded by the strong mixing at the leading edge, and at the top of the shallow cold pool. The wave breaks when the pool is completely flushed out as indicated in Fig. 9. The everywhere-subcritical pattern shown in Fig. 8 is not found in Fig. 9 since the cold pool is inefficient in inhibiting the eventual development of the mountain waves, although the time of onset is delayed.

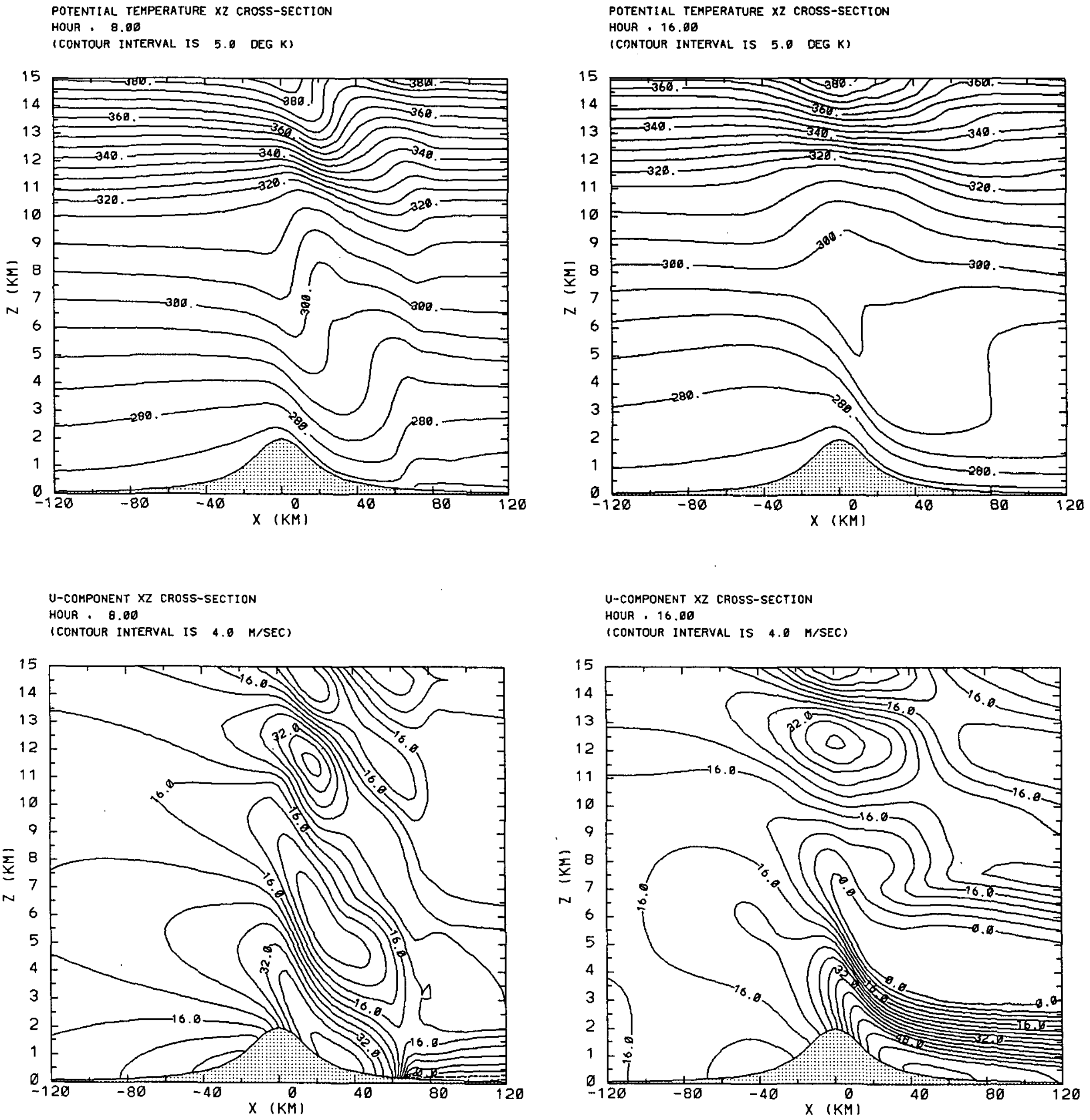

FIG. 9. As in Fig. 8 except that the cold pool is 1000 m deep.

In a case where there is a large-scale geostrophic wind in the cold pool directing air away from the mountain (i.e., $U_g > 0$ within the cold pool), the cold pool moves immediately after initialization away from the barrier. The result of this simulation (not shown here) is very similar to Fig. 4.

The results in this section suggest that our first hypothesis that the mountain induced wave, due to just the terrain configuration, can flush out the cold pool is not appropriate since the depth of the cold pool is important in determining the structure of the mountain wave and its resistance to erosion. This hypothesis should work only when the cold pool is relatively shallow and the mountain wave structure is not greatly modified by the cold pool. On the other hand, the results strongly suggest the orientation of the surface synoptic pressure gradient force, and hence the associated surface geostrophic wind direction, is very significant in determining the rate of downslope development of a downslope wind storm when a cold pool is present initially. When the geostrophic wind in the cold pool is directed away from the mountain, downslope wind development is favored. The general surface pressure pattern associated with this geostrophic wind is low pressure to the north and high pressure to the south. On the other hand, when the geostrophic wind is directed toward the mountain, which favors the damming of the cold pool, downslope wind development is inhibited. The general surface pressure pattern associated with this geostrophic wind is low pressure to the south and high pressure to the north. Although the upstream stratification and the flow at ridge top height can be similar in either of the cases, very different weather will be experienced along the lee slope of the mountain. Although the cold pool along the lee slope can be slowly eroded away on its windward side by the mountain-induced wave flow, the orientation of the synoptic pressure gradient force is much more efficient at eliminating the layer of cold near-surface air.

A recent statistical compilation of synoptic variables associated with downslope windstorms (see Appendix) has shown that the most favorable synoptic scale surface pressure pattern associated with severe downslope windstorms in northeast Colorado is high pressure to the southwest, and low pressure to the northeast. A strong northerly geostrophic wind component is often experienced at the surface during the windstorms. To examine the role played by the northerly wind, a series of simulations with different northerly geostrophic wind speeds are performed. It is found that when the northerly component is small, as expected the flow patterns are almost identical to the run without the northerlies as shown in Fig. 4. However, very different results are found when the northerlies are strong. In Fig. 10 a run is presented at $\bar{u}t/a = 28.8$ (the same time as shown in Fig. 4 experiment), except with a 20 m s^{-1} northwesterly geostrophic wind. By comparing Fig. 10 to Fig. 4, the surface westerly wind is stronger even with a weaker westerly component of geostrophic wind. It is believed that the stronger westerly component is due to the turning of winds towards low pressure in response to the wave drag.

To isolate the contribution to flushing process due to turbulent mixing, one more experiment is performed. The model is initialized with neutrally stratified flow except with a 2 km cold pool downstream of the mountain. A zero geostrophic wind is assigned in the cold pool. Since the environment is neutral, no wave is expected to form and the only way to flush out the cold pool is mixing. As indicated in Fig. 11, the streamlines are parallel to each other and the cold pool retains its depth and position even after a dimensionless time of $\bar{u}t/a = 28.8$. This result further demonstrates that the mixing process is relatively unimportant in removing a cold pool as compared to the removal of cold air by advection away from the barrier.

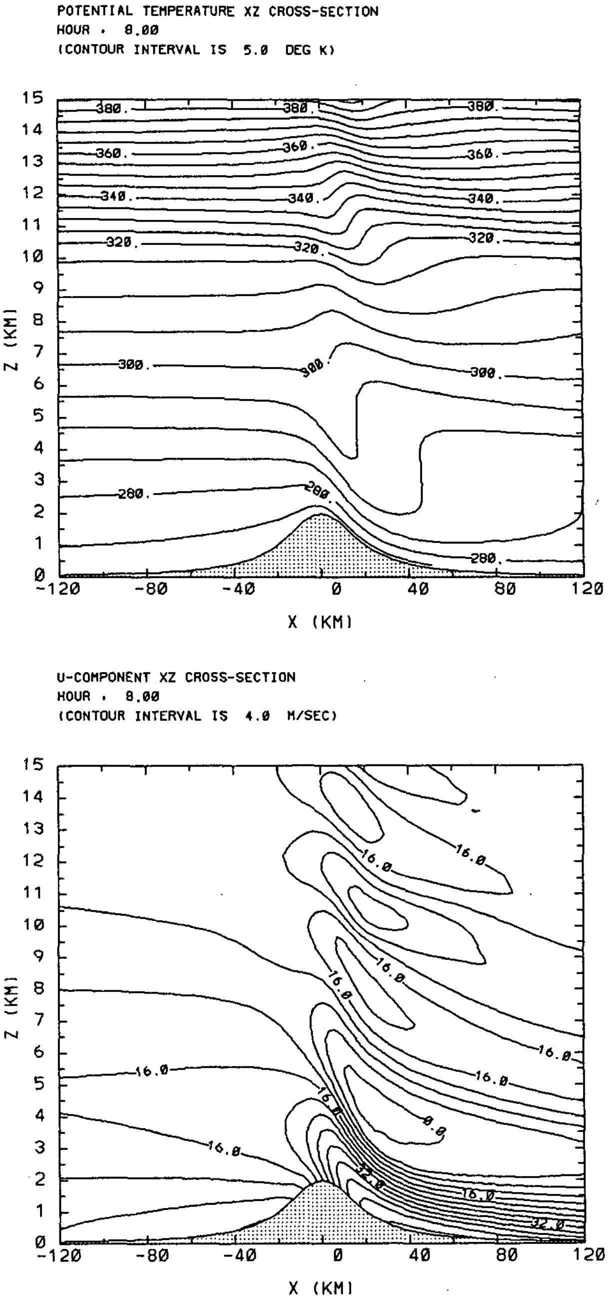
POTENTIAL TEMPERATURE XZ CROSS-SECTION
HOUR . 8.00
(CONTOUR INTERVAL IS 5.0 DEG K)

U-COMPONENT XZ CROSS-SECTION
HOUR . 8.00
(CONTOUR INTERVAL IS 4.0 M/SEC)

FIG. 10. Same as Fig. 4 except the cross mountain flow is 20 m s^{-1} from the northwest.

5. Conclusions

In this paper we have examined the importance of the orientation of the synoptic surface pressure pattern and the influence of a cold pool downstream of a bell-shaped mountain on the generation of downslope wind storms. A mesoscale numerical model has been applied to perform the analysis. The numerical model is found to accurately reproduce the phase and amplitude of

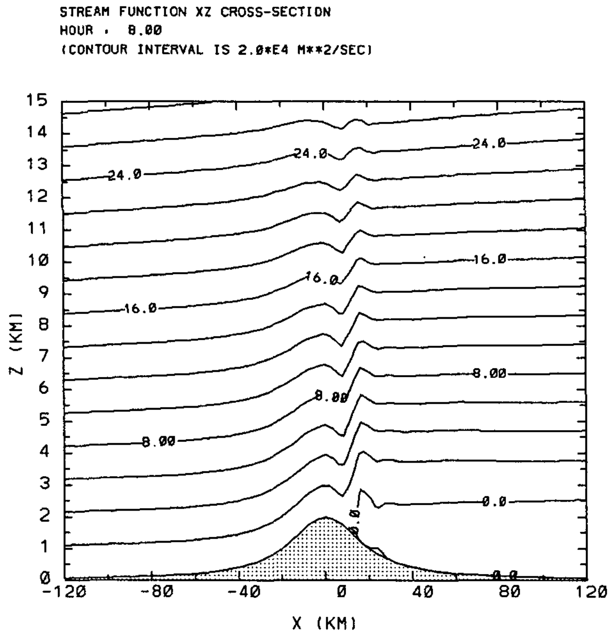

FIG. 11. Numerical solution for streamlines at $\bar{u}t/a = 28.8$ for a neutrally stratified atmosphere flowing over a mountain with $h = 1000$ m and a 2000 m deep cold pool with $N = 0.02$ s^{-1} downstream of the mountain.

linear and nonlinear hydrostatic mountain waves over both a symmetric bell-shaped mountain and an asymmetric mountain. The effect of different atmosphere structure on the mountain waves is also tested. The result shows a good replication of the work reported by Durran (1986).

When a pool of cold and stable air is present downstream of the mountain, it is found that the cold pool can modify the mountain waves very significantly, not only near the surface but also the wave structure aloft. Several features associated with the presence of the cold pool are:

1) The top of the cold pool acts very much like terrain with similar shape.

2) The core of maximum horizontal wind moves from the lee slope toward the top of the mountain.

3) The downslope wind along the lee slope is limited in downstream propagation.

4) The flow resembles an everywhere-subcritical pattern.

5) Compared to the direct effect of the forced mountain wave near the surface, the orientation of the synoptic pressure gradient force is more efficient at flushing the cold pool and in the development of strong downslope winds along the lee slope.

6) Flushing of the cold pool by a forced mountain wave can occur only when the cold pool is shallow.

7) Turbulent mixing at the top of the cold pool is relatively unimportant.

It is also concluded that strong downslope winds cannot reach the surface before the cold and stable air is flushed out. Until this cold air is removed, the mountain wave structure is significantly modified from what it otherwise would be. Based on the observational and numerical simulation results, in the absence of surface heating, a surface geostrophic wind directed away from the terrain barrier must be present in order for a deep cold pool to be advected away from the terrain and to permit downslope winds to move to lower elevations on the lee slope.

Acknowledgments. We wish to express our gratitude to Raymond Arritt and Mordecay Segal for their helpful comments and suggestions which led to the completion of this study. We would also like to thank Dennis Rogers (WRG/ERL) for his help in filling in some of the missing data bins. This research was supported by NSF Grant ATM-8616662 and NOAA/ERL Grant NA-85-RAH-05045. Computational facilities were provided by NCAR's Scientific Computing Division which is also acknowledged. NCAR is sponsored by the National Science Foundation.

APPENDIX

The following table is a listing of about two-thirds of the synoptic variables compiled for 71 cases of severe downslope windstorms in Fort Collins, Colorado. The footnote to the table gives the authors' definition of severe.

The data for the ten year period were accumulated to develop what at first was a simple forecast checklist. This concept evolved into an expert system application which analyzes downslope wind events in Fort Collins. Thus, many of the parameters are forecaster oriented, and refer to the routinely available synoptic set of maps. Note, however, the consistency of many of the variables from case to case. In particular, notice the high frequency of occurrence for cases in which the surface geostrophic wind direction is between 330 and 030.

It is interesting to note that of over thirty separate variables tested, only two seemed to be of first-order importance in forecasting the occurrence of severe downslope winds in Fort Collins. These are 1) the surface geostrophic wind (speed and direction), and 2) the 700 mb geostrophic wind (speed and direction). Also, it was found that the onset of negative 500 mb vorticity advection seemed to be associated with the start of the downslope winds in about 40 percent of the cases. Finally, subjective indications (before the present study was undertaken) were that the presence of deep cold pools seems to impede downslope outbreaks entirely, in all cases except those in which both the surface and 700 mb gradients are unusually strong.

Severe Downslope Wind Events in Fort Collins, Colorado for the Period September 1977

Date	Strength*	Surface geostrophic direction	Approximate surface geostrophic speed (kts)	Surface† gradient per 400 km	Approximate position closest surface low (lat/long)	Approximate position closest surface high (lat/long)	Temperature before/after (°C)	700 mb geostrophic direction (deg)	Approximate 700 mb geostrophic speed (kt)	700 mb† gradient per 400 km
17/18 Jun 1973††	15	30	34	4	40/100	43/122	—	290	20	2.5
23 Sep 1977	10	360	30	3.5	42/102	41/115	—	270	16	2
26 Nov 1977	18	330	34	4	50/111	36/110	—	300	24	3
2 Dec 1977	30	330	34	4	41/102	36/110	—	310	31	4
3 Dec 1977	2	330	26	3	47/109	36/110	—	300	24	3
4 Dec 1977	3	320	26	3	42/105	—	—	300	20	2.5
7 Dec 1977	2	300	34	4	43/107	36/109	—	290	28	3.5
29 Nov 1977	2	360	34	4	39/104	38/111	—	300	24	3
16 Dec 1977	3	360	34	4	40/98	39/118	—	340	24	3
22 Dec 1977	2	340	43	5	40/102	36/109	—	300	24	3
23 Dec 1977	9	340	34	4	43/105	38/108	—	290	24	3
24 Dec 1977	15	340	34	4	41/97	38/118	—	310	24	3
22/23 Nov 1978	3	360	26	3	42/103	40/117	—	290	16	2
4 Dec 1978	3	320	34	4	57/94	37/111	—	310	31	4
21 Dec 1978	2	350	34	4	51/98	40/117	—	310	20	2.5
23 Dec 1978	2	340	26	3	46/99	40/119	—	310	24	3
24 Dec 1978	9	320	30	3.5	58/115	40/118	—	310	24	3
7 Feb 1979	6	310	34	4	45/107	38/109	—	310	24	3
4/5 Dec 1979	4	340	51	6	50/97	38/109	—	310	24	3
15 Dec 1979	4	340	43	5	45/99	38/109	—	310	20	2.5
6 Jan 1980	2	340	51	6	44/102	37/110	—	290	24	3
10/11 Jan 1980	11	350	26	3	46/97	42/116	—	310	24	3
24 Jan 1980	2	360	34	4	46/95	43/118	—	320	20	2.5
12 Mar 1980	2	20	34	4	40/103	—	—	320	16	2
7 Apr 1980	9	20	26	3	45/96	42/120	—	300	16	2
24 Dec 1980	*6*	*200*	*26*	*3*	*41/107*	*37/110*	—	*300*	*20*	*2.5*
8 Feb 1981	2	350	17	2	42/105	39/116	—	300	24	3
31 Mar 1981	4	350	26	3	43/97	40/113	—	320	24	3
3 Jan 1982	18	350	26	3	48/110	37/110	—	320	24	3
14 Jan 1982	6	330	39	4.5	51/102	39/111	—	310	24	3
17 Jan 1982	16	330	43	5	48/106	36/110	—	300	31	4
24 Jan 1982	44	350	43	5	47/104	40/116	—	310	28	3.5
9 Mar 1982	3	330	17	2	54/105	40/110	—	300	16	2
10 Mar 1982	7	330	17	2	47/97	35/110	—	300	16	2
12 Mar 1982	10	20	26	3	40/102	43/119	—	270	24	3
29/30 Mar 1982	29	340	30	3.5	43/101	—	—	310	24	3
2 Apr 1982	34	20	43	5	41/101	—	—	330	35	4.5
9 Oct 1982	9	360	43	5	44/98	49/116	—	350	28	4
18 Dec 1982	2	360	22	2.5	48/95	40/113	2.5/5.0	300	20	2.5
6 Jan 1983	3	310	43	5	47/103	37/109	12/15	300	24	3
8/9 Jan 1983	15	350	43	5	42/100	40/116	4/12	290	24	3
10 Feb 1983	2	350	17	2	42/102	40/110	—	320	16	2
19 Feb 1983	5	30	34	4	38/101	42/118	2/7	10	20	2.5
30 Mar 1983	15	300	22	2.5	52/106	35/112	12/14	300	20	2.5
13 Nov 1983	2	330	14	1.5	45/102	42/112	−2/6	290	16	2
6 Dec 1983	2	340	17	2	47/110	37/110	—	320	16	2
8 Dec 1983	2	330	26	3	42/104	35/109	2/11	290	24	3
10 Dec 1983	3	350	17	2	42/102	37/111	5/8	320	16	2
11 Apr 1984	5	360	26	3	45/100	44/118	5/8	310	16	2
1 Dec 1984	3	10	17	2	42/102	44/115	−2/4	310	16	2
22/23 Dec 1984	15	330	43	5	43/104	39/112	0/8	300	28	3.5
23 Mar 1985	3	330	17	2	43/94	37/110	4/6	310	16	2
26 Mar 1985	3	30	26	3	40/104	42/113	6/14	290	16	2
19 Apr 1985	8	350	43	5	41/103	40/114	12/14	310	28	3.5
23/24 Jan 1986	9	10	34	4	38/102	43/122	6/16	320	16	2
15 Feb 1986	35	350	34	4	42/105	32/108	4/13	270	24	3
16 Feb 1986	6	310	26	3	44/107	—	5/8	300	24	3
19 Feb 1986	4	300	26	3	43/107	—	4/15	260	24	3
22 Feb 1986	3	330	30	3.5	42/105	38/111	12/12	290	24	3
23 Feb 1986	12	330	22	2.5	42/105	37/111	10/10	300	24	3
4 Mar 1986	6	350	34	4	45/96	45/117	10/14	310	16	2
13 Apr 1986	5	360	34	4	41/101	—	—	310	24	3
4/5 May 1986	31	350	30	3.5	47/100	41/115	—	310	24	3
24 Jan 1987	2	330	26	3	43/104	37/112	—	310	12	1.5
26/27 Jan 1987	7	310	26	3	—	38/110	—	310	16	2
28/29 Jan 1987	11	340	34	4	43/102	41/114	—	310	20	2.5
2 Feb 1987	2	340	34	4	49/103	37/109	—	310	20	2.5
2 Dec 1987	18	330	26	3	43/100	38/110	0/8	310	16	2
11 Jan 1988	12	350	34	4	44/103	—	−2/7	290	24	3

through January 1988—Various Associated Meteorological Parameters.

500 mb geostrophic direction	Approximate 500 mb geostrophic speed	500 mb† gradient per 400 km	300 mb geostrophic direction	300 mb† gradient per 400 km	Longwave: trough (T) ridge (R) neutral (N)	Location of 300 mb wind Max (O = Ovrhd N = north, S = south, etc)	500 mb temp (C) Den/ upwind	Time of downslope winds begin/end (All)	Time of downslope winds begin/end (severe)**	Time of max gust (LST)	Strength of max gust (kt)	500 mb vorticity advection [×(10)⁻¹ s⁻¹]
240	39	2.5	240	2.5	N	—	−12/−14	0830/0400	2115/1200	245	79	—
240	31	2	240	1.5	T	O	−10/−20	0400/1645	0530/1430	1130	68	—
290	31	2	300	1	R	N	−16/−15	0115/XXX	0130/1330	230	71	—
310	39	2.5	320	1.5	R	N	−19/−16	0330/XXX	0445/2345	1400	66	—
300	31	2	300	1.5	R	N	−15/−15	XXX/XXX	0615/1745	1630	52	—
290	31	2	310	2	R	NW	−22/−24	1100/XXX	1245/2230	2115	64	—
300	31	2	300	1.5	R	NW	−18/−18	0700/XXX	0715/1145	830	54	—
280	31	2	280	2	R	NW	−18/−19	2030/XXX	2200/2345	2300	63	—
300	16	1	300	0.5	R	SW	−22/−30	XXX/XXX	1015/2100	1930	57	—
280	31	2	280	1	R	SW	−16/−19	0745/XXX	0815/0415	100	67	—
290	31	2	280	1	R	S	−22/−22	1330/XXX	1430/0000	1430	55	—
300	31	2	290	1.5	R	S	−24/−25	XXX/0945	0000/0915	430	66	—
270	31	2	250	2	N	SW	−22/−22	1315/XXX	1900/0630	530	53	—
310	47	3	310	1.5	R	N	−20/−16	0945/XXX	1045/1645	1130	56	—
290	31	2	300	1.5	R	N	−22/−25	1330/1815	1400/1815	1800	54	—
280	31	2	270	1.5	R	NW	−26/−27	XXX/XXX	0045/0345	200	53	—
310	39	2.5	310	2	R	NW	−16/−17	0930/XXX	1000/2045	1100	64	—
300	31	2	310	1.5	R	NW	−23/−22	1130/2300	1200/2130	1300	68	—
270	31	2	270	1.5	R	N	−10/−14	2200/XXX	2230/0645	15	61	—
310	16	1	280	0.5	R	N	−20/−15	0500/1130	0530/1115	645	56	—
270	39	2.5	270	2	R	O	−14/−16	XXX/XXX	0030/0145	115	54	—
290	47	3	290	2	N	NW	−24/−30	0930/0500	0945/0445	245	68	—
310	39	2.5	300	2	R	NW	−16/−18	1345/XXX	1400/1745	1730	57	—
290	24	1.5	280	0.5	R	S	−24/−25	0720/XXX	1000/1330	1215	53	—
250	24	1.5	260	1.5	R	W	−25/−28	0200/XXX	0615/2100	1400	58	—
310	31	2	310	1.5	R	E	−19/−20	0330/XXX	1715/1945	1815	65	—
300	39	2.5	300	2	R	NE	−22/−23	1245/XXX	1300/1500	1415	52	−1
330	31	2	280	1	N	SE	−29/−28	0230/1700	0315/1115	730	55	−4
310	24	1.5	310	1.5	N	NW	−34/−37	XXX/2030	XXX/0203	1900	74	−4
300	31	2	300	1.5	R	NW	−22/−26	1330/XXX	1345/1715	1615	64	−2
290	47	3	290	1.5	R	NW	−10/−16	0045/XXX	0100/1330	415	65	0
300	39	2.5	300	2	R	NW	−14/−15	0710/2030	0730/2000	1030	83	—
300	24	1.5	290	1	N	W	−23/−22	0900/XXX	1115/1630	1115	55	−4
290	31	2	300	1.5	R	NE	−16/−19	XXX/1745	0600/1645	1130	62	−2
240	39	2.5	240	2	T	SW	−17/−20	0300/XXX	0330/1615	1015	62	−2
270	16	1	210	1	T	S	−23/−29	1730/0445	0800/0430	2300	74	−6
280	31	2	270	1.5	N	S	−21/−31	0600/0140	0615/2245	1100	78	—
10	24	1.5	XXX	—	R	SE	−23/−20	XXX/XXX	0800/2015	1245	60	−4
290	39	2.5	270	2	N	S	−28/−25	0210/1810	0915/1115	1000	53	—
300	31	2	300	1	R	N	−15/−17	0000/1200	0030/0430	345	61	—
290	31	2	270	1	R	S	−18/−25	1810/1900	2145/1545	845	68	—
310	16	1	310	1	N	S	−24/−27	XXX/1050	0330/0600	600	55	−4
20	24	1.5	20	1	T	SW	—	0545/XXX	1015/1715	1430	56	−4
300	31	2	290	1	R	NW	−21/−19	1100/2230	1130/1730	1315	72	−2
280	24	1.5	270	1.5	N	O	−17/−20	0730/1500	0800/1230	815	58	−2
310	31	2	310	2	R	SE	−34/−34	0120/1630	0145/0445	245	53	−2
280	31	2	280	2	N	NW	−16/−20	0700/XXX	0830/1000	845	53	0
310	16	1	—	—	R	—	−21/−24	1800/XXX	1900/2130	2115	56	—
300	24	1.5	290	2	T	SW	−25/−30	0010/0730	1315/0100	1530	60	−2
270	31	2	270	1.5	N	SW	−24/−24	0230/1615	0830/1230	1030	54	—
290	39	2.5	290	2.5	R	N	−19/−21	0230/0715	0130/1445	645	65	—
310	39	2.5	320	2	R	NW	−27/−26	1030/1515	0730/2200	1115	56	−4
250	24	1.5	270	1	T	SE	−23/−22	XXX/1930	1400/1645	1545	62	—
300	31	2	250	0.5	T	SE	−16/−19	1100/1800	1145/1630	1415	64	−4
280	31	2	270	1.5	N	SE	−16/−17	1330/XXX	2330/0545	515	64	−4
260	47	3	260	1	R	NE	−13/−17	0415/1700	0445/1700	1015	73	0
290	24	1.5	290	0.5	N	SW	−22/−23	0530/2030	0800/1700	1600	57	−2
260	39	2.5	260	2	N	N	−16/−17	0830/XXX	0930/1130	1115	58	0
300	31	2	300	1.5	R	NW	−21/−21	1330/XXX	1400/2000	1800	56	−2
310	31	2	310	1.5	R	NW	−20/−21	XXX/0745	2345/0615	500	64	0
300	31	2	310	1	R	N	−16/−17	2000/0700	2130/0115	2200	65	0
280	31	2	270	1.5	T	S	−15/−22	0700/1830	0715/1515	1215	64	4
270	31	2	240	1.5	T	O	−14/−17	1800/1245	1930/1215	2115	78	−3
310	16	1	310	1	R	SE	−22/−22	2100/1730	2215/2345	2300	57	−2
310	31	2	310	1.5	R	N	−23/−19	XXX/XXX	XXX/0330	330	56	—
270	24	1.5	260	1.5	N	SE	−20/−21	1600/1345	1745–0715	30	73	—
290	31	2	270	1	N	N	−16/−14	2300/0300	0130–0245	245	54	0
300	24	1.5	300	1	R	NW	−18/−18	1015/0215	1330–0130	1515	73	−2
260	31	2	240	2	N	O	−20/−22	0615/1700	0830–0245	1900	61	−2

(continued).

Date	Strength*	Surface geostrophic direction	Approximate surface geostrophic speed (kts)	Surface† gradient per 400 km	Approximate position closest surface low (lat/long)	Approximate position closest surface high (lat/long)	Temperature before/after (°C)	700 mb geostrophic direction (deg)	Approximate 700 mb geostrophic speed (kt)	700 mb† gradient per 400 km
15/16 Jan 1988	4	350	34	4	52/101	40/112	0/9	300	16	2
23 Jan 1988	8	360	43	5	46/101	39/113	−6/5	320	28	3.5
Average (all)		342	31	3.6	44.3/102.2	39.1/113.0	4.2/10.0	305	21.9	2.7
Total cases		71	71	71	70	63	25	71	71	71
Std dev		±27	±8.6	±1	±4.1/4.1	±2.9/3.7	±4.9/3.6	±16.5	±4.7	±0.6
Range		200–030	14–51	1.5–6	38–58/94–115	32–49/108–122	(−6)–12/4–16	260–010	12–35	15–4.5
Average (≥9)		348	33	3.8	44.3/102.8	39.5/114.4		303	26.6	3
Total cases		25	25	25	25	22		25	25	25
Std dev		±21	±6.4	±0.8	±4.2/4.3	±3.6/4.3		±17.8	±4.7	±0.16
Range		300–030	22–43	2.5–5	38–58/96–115	32–49/108–122		270–350	16–35	2–4.5

* The strength of the outbreak was determined by graphically estimating the area beneath a plot of 15 minute maximum wind gust versus time, and above the 45 knot line. (All of the events were gusty in nature.) The definition is arbitrary and was originally made in order to scale the outbreaks relative to one another.

** A severe downslope event is arbitrarily defined as one in which multiple wind gusts exceed 44 kts for 30 minutes, or longer.

† Gradient per 400 km—The gradient increments referred to are the standard NMC gradients for each level (i.e., 4 mb at the surface, 30 meters at 700 mb, 60 meters at 500 mb, and 120 meters at 300 mb). The value shown is the number of such increments found in a 400 km distance. 400 km was chosen because that is the distance from the northwest corner of Colorado to the southeast corner of Wyoming, and is easily determined on any scale synoptic map.

†† Extra case included in the main dataset.

500 mb geostrophic direction	Approximate 500 mb geostrophic speed	500 mb[†] gradient per 400 km	300 mb geostrophic direction	300 mb[†] gradient per 400 km	Longwave: trough (T) ridge (R) neutral (N)	Location of 300 mb wind Max (O = Ovrhd N = north, S = south, etc)	500 mb temp (C) Den/upwind	Time of downslope winds begin/end (All)	Time of downslope winds begin/end (severe)[**]	Time of max gust (LST)	Strength of max gust (kt)	500 mb vorticity advection $[\times(10)^{-1}\ s^{-1}]$
250	31	2	—	—	N	—	−16/−19	1400/0615	1500–0530	1515	55	−2
300	47	3	—	—	R	—	−15/−17	0245/XXX	0300–0800	400	63	−4
291.1	31	2	285.2	1.5			−19.7/−21.4					
71	71	71	67	67			70					
±24.3	±7.6	±0.5	±26.1	±0.5			±4.9/5.0					
240–020	16–47	3-Jan	210–020	0.5–25			(−10)–(−34)/ (−14)–(−37)					
284.8	32.5	2.1	274	1.5			−18.8/−21.3					
25	25	25	24	24			25					
28.3	±7.7	±0.5	±28.6	±0.4			±5.3/5.8					
240–010	16–47	3-Jan	*210–320*	*1–2.5*			(−10)–(−34)/ (−14)–(−37)					

REFERENCES

Bacmeister, J. T., and R. T. Pierrehumbert, 1988: On high-drag states of nonlinear stratified flow over an obstacle. *J. Atmos. Sci.*, **45,** 63–80.

Clark, T. L., and W. R. Peltier, 1977: On the revolution and stability of finite-amplitude mountain waves. *J. Atmos. Sci.*, **34,** 1715–1730.

——, and ——, 1984: Critical level reflection and the resonant growth of nonlinear mountain waves. *J. Atmos. Sci.*, **41,** 3122–3134.

Durran, D. R., 1986: Another look at downslope windstorms. Part I: The development of analogs to supercritical flow in an infinitely deep, continuously stratified fluid. *J. Atmos. Sci.*, **43,** 2527–2543.

——, and J. B. Klemp, 1982: The effects of moisture on trapped mountain lee waves. *J. Atmos. Sci.*, **39,** 2341–2361.

——, and ——, 1987: Another look at downslope winds. Part II: Nonlinear amplification beneath wave-overturning layers. *J. Atmos. Sci.*, **44,** 3402–3412.

Hoinka, K. P., 1985: A comparison of numerical simulations of hydrostatic flow over mountains with observations. *Mon. Wea. Rev.*, **113,** 719–735.

Klemp, J. B., and D. K. Lilly, 1978: Numerical simulation of hydrostatic mountain waves. *J. Atmos. Sci.*, **35,** 78–107.

Lilly, D. K., and J. B. Klemp, 1979: The effects of terrain shape on nonlinear hydrostatic mountain waves. *J. Fluid Mech.*, **95,** 241–261.

McNider, R. T., and R. A. Pielke, 1981: Diurnal boundary-layer development over sloping terrain. *J. Atmos. Sci.*, **38,** 2198–2212.

Mahrer, Y., 1984: An improved numerical approximation of the horizontal gradients in a terrain-following coordinate system. *Mon. Wea. Rev.*, **112,** 918–922.

——, and R. A. Pielke, 1977: A numerical study of the air flow over irregular terrain. *Contrib. Atmos. Phys.*, **50,** 98–113.

——, and R. A. Pielke, 1978: A test of an upstream spline interpolation technique for the advective terms in a numerical mesoscale model. *Mon. Wea. Rev.*, **106,** 818–830.

Miles, J. W., and H. E. Huppert, 1969: Lee waves in a stratified flow. Part 4. Perturbation approximations. *J. Fluid Mech.*, **35,** 497–525.

Peltier, W. R., and T. Clark, 1979: The evolution and stability of finite amplitude mountain waves. Part II: Surface wave drag and severe downslope windstorms. *J. Atmos. Sci.*, **36,** 1498–1529.

Pielke, R. A., 1974: A three dimensional numerical model of the sea breeze over south Florida. *Mon. Wea. Rev.*, **102,** 115–139.

——, 1984: *Mesoscale Meteorological Modeling.* Academic Press, 612 pp.

——, 1985: The use of mesoscale models to assess wind distribution and boundary-layer structure in complex terrain. *Bound. Layer Meteor.*, **31,** 217–231.

Pierrehumbert, R. T., and B. Wyman, 1985: Upstream effects of mesoscale mountains. *J. Atmos. Sci.*, **42,** 977–1003.

Smith, R. B., 1985: On severe downslope winds. *J. Atmos. Sci.*, **42,** 2597–2603.